Fermi Gamma-ray Imaging of a Radio Galaxy

The Fermi-LAT Collaboration*

The *Fermi* Gamma-ray Space Telescope has detected the γ-ray glow emanating from the giant radio lobes of the radio galaxy Centaurus A. The resolved γ-ray image shows the lobes clearly separated from the central active source. In contrast to all other active galaxies detected so far in high-energy γ-rays, the lobe flux constitutes a considerable portion ($>$1/2) of the total source emission. The γ-ray emission from the lobes is interpreted as inverse Compton scattered relic radiation from the cosmic microwave background (CMB), with additional contribution at higher energies from the infrared-to-optical extragalactic background light (EBL). These measurements provide γ-ray constraints on the magnetic field and particle energy content in radio galaxy lobes, and a promising method to probe the cosmic relic photon fields.

Cen A is one of the brightest radio sources in the sky and was amongst the first identified with a galaxy (NGC 5128) outside of our Milky Way (*1*). Straddling the bright central source is a pair of extended radio lobes with a total angular extent of $\sim$10° (*2,3*), which makes Cen A the largest discrete non-thermal extragalactic radio source visible from the Earth. At a distance 3.7 Mpc (*4*), it is the nearest radio galaxy to us, and the implied physical source size is $\sim$600 kpc. Such double-lobed radio structures associated with otherwise apparently normal giant elliptical galaxies have become the defining feature of radio galaxies in general. The consensus

*All authors with their affiliations appear at the end of this paper.

explanation for this phenomenon is that the lobes are fueled by relativistic jets produced by accretion activity in a super-massive black hole residing at the galaxy's center.

With its unprecedented sensitivity and imaging capability (per-photon resolution, $\theta_{68} \simeq 0^{\circ}.8\, E_{\rm GeV}^{-0.8}$), the $Fermi$ Large Area Telescope (LAT) (*5*) has detected and imaged the radio lobes of Cen A in high-energy γ-rays. The LAT image resulting from $\sim$10 months of all-sky survey data (Fig. 1) clearly shows the γ-ray peak coincident with the active galactic nucleus (AGN) detected by the *Compton/EGRET* instrument (*6*) and extended emission from the southern giant lobe. Because the northern lobe is characterized by lower surface brightness emission (in radio), it is not immediately apparent from a by-eye inspection of the γ-ray counts map. Nevertheless, from a counts profile extracted along the north-south axis of the source (Fig. 2) γ-ray excesses from both lobes are clearly visible.

Spectra for each of the lobes together with the central source (hereafter, the "core") were determined with a binned maximum likelihood analysis implemented in `GTLIKE` (*7*) using events from 0.2–30 GeV in equal logarithmically spaced energy bins. Background emission was modeled by including the Galactic diffuse component, an isotropic component, and nearby γ-ray point sources (SOM). We fit the core as a point source at the known radio position and the lobe emission was modeled using a 22 GHz WMAP image ((*8*); Fig. 1) with the core region within a 1° radius excluded as a spatial template. The modeled lobe region roughly corresponds to the region 1 & 2 (north), and 4 & 5 (south) defined in (*9*), where region 3 is the core (Fig. 2). Assuming a power-law for the γ-ray spectra, we find a large fraction ($>$1/2) of the total $>$100 MeV emission from Cen A to originate from the lobes with the flux in each of the northern ((0.77 (+0.23/–0.19)$_{\rm stat.}(\pm 0.39)_{\rm syst.}) \times 10^{-7}$ ph cm^{-2} s^{-1}) and southern ((1.09 (+0.24/–0.21)$_{\rm stat.}(\pm 0.32)_{\rm syst.}) \times 10^{-7}$ ph cm^{-2} s^{-1}) lobes smaller than the core flux ((1.50 (+0.25/–0.22)$_{\rm stat.}(\pm 0.37)_{\rm syst.}) \times 10^{-7}$ ph cm^{-2} s^{-1}). Uncertainties in the LAT effective area, the Galactic diffuse model used, and the core exclusion region were considered as sources of

systematic error (SOM). The resultant test statistic (TS; (*10*)) for the northern and southern giant lobes are 29 and 69, which corresponds to detection significances of 5.0σ and 8.0σ, respectively. The lobe spectra are steep, with photon indices, Γ = 2.52 (+0.16/–0.19)$_{\rm stat.}(\pm 0.25)_{\rm syst.}$ (north) and 2.60 (+0.14/–0.15)$_{\rm stat.}(\pm 0.20)_{\rm syst.}$ (south) where photons up to ∼2–3 GeV are currently detected. These values are consistent with that of the core ($\Gamma = 2.67\ (\pm 0.10)_{\rm stat.}(\pm 0.08)_{\rm syst.}$) which is known to have a steep γ-ray spectrum (*6*). For further details pertaining to the analysis of the lobe emission see the SOM.

It is well-established that radio galaxy lobes are filled with magnetized plasma containing ultra-relativistic electrons emitting synchrotron radiation in the radio band (observed frequencies, $\nu \sim 10^7 - 10^{11}$ Hz). These electrons also up-scatter ambient photons to higher energies via the inverse Compton (IC) process. At the observed distances far from the parent galaxy (>100 kpc-scale), the dominant soft photon field surrounding the extended lobes is the pervading radiation from the CMB (*11*). Because IC/CMB scattered emission in the lobes of more distant radio galaxies is generally well observed in the X-ray band (*12–14*), the IC spectrum can be expected to extend to even higher energies (*9, 15*), as demonstrated by the LAT detection of the Cen A giant lobes.

To model the observed lobe γ-rays as IC emission, detailed radio measurements of the lobes' synchrotron continuum spectra are necessary to infer the underlying electron energy distribution (EED), $n_{\rm e}(\gamma)$, where the electron energy is $E_{\rm e} = \gamma m_{\rm e} c^2$. In anticipation of these $Fermi$ observations, ground-based (*16, 17*) and WMAP satellite (*8*) maps of Cen A were previously analyzed (*9*). Here, we separately fit the $0.4 - 60$ GHz measurements for each region defined therein for the north (1 and 2) and south (4 and 5) lobes (see Fig. 2) with EEDs in the form of a broken power-law (with normalization $k_{\rm e}$ and slopes s_1 and s_2) plus an exponential cutoff at high energies: $n_{\rm e}(\gamma) = k_{\rm e}\,\gamma^{-s_1}$ for $\gamma_{\rm min} \leq \gamma < \gamma_{\rm br}$ and $n_{\rm e}(\gamma) = k_{\rm e}\,\gamma_{\rm br}^{s_2 - s_1}\,\gamma^{-s_2}\,\exp[-\gamma/\gamma_{\rm max}]$ for $\gamma \geq \gamma_{\rm br}$, such that the electron energy density is $U_{\rm e} = \int E_{\rm e}\, n_{\rm e}(\gamma)\, d\gamma$. To a certain extent,

our modeling results depend on the shape of the electron spectrum at energies higher than those probed by the WMAP measurements ($\nu \gtrsim 60$ GHz; Fig. 3); we have assumed the spectrum to decline exponentially.

The IC spectra resulting from the fitted EED (parameters listed in Table S1 of the SOM) were calculated employing precise synchrotron (*18*) and IC (*19*) kernels (including Klein-Nishina effects) by adjusting the magnetic field, B. In addition to the CMB photons, we included IC emission off the isotropic infrared-to-optical EBL radiation field (*9, 20, 21*), utilizing the data compilation of (*22*). Anisotropic radiation from the host galaxy starlight and the well-known dust lane was also included, but was found to have a negligible contribution in comparison to the EBL (Fig. 4, see also the SOM). The resultant total IC spectra of the northern and southern lobes (Fig. 3) with $B = 0.89\,\mu$G (north) and $B = 0.85\,\mu$G (south) provide satisfactory representations of the observed γ-ray data. These B-field values imply that the high-energy γ-ray emission detected by the LAT is dominated by the scattered CMB emission, with the EBL contributing at higher energies ($\gtrsim 1$ GeV; Fig. 4).

Considering only contributions from ultra-relativistic electrons and magnetic field, the lobe plasma is found to be close to the minimum energy condition with the ratio of the energy densities, $U_{\rm e}/U_{\rm B} \simeq 4.3$ (north) and $\simeq 1.8$ (south), where $U_{\rm B} = B^2/8\pi$. The EED was assumed to extend down to $\gamma_{\rm min} = 1$; adopting larger values can reduce this ratio by a fractional amount for the south lobe, and up to $\sim 2\times$ for the north lobe (SOM). For comparison, IC/CMB X-ray measurements of extended lobes of more powerful (FRII) radio sources have been used to infer higher B-fields and equipartition ratios with a range $U_{\rm e}/U_{\rm B} \simeq 1 - 10$ (*12–14*).

The radiating particles in the Cen A lobes lose energy predominantly through the IC channel, because the ratio of the corresponding cooling times is equal to the energy density ratio, $U_{\rm CMB}/U_{\rm B} \gtrsim 10$. This manifests itself in the $\sim$order of magnitude dominance of the γ-ray component over the radio one in the observed SEDs (Fig. 3). However, the magnetic field con-

straints (thus the exact ratios of $U_{\rm CMB}/U_{\rm B}$) are sensitive to the shape of the EED at the electron energies, $E_{\rm e} > 0.1$ TeV. On one hand, magnetic field strengths greater than $B{\sim}1$ μG will underproduce the observed LAT emission for all reasonable forms of the EED, so the quoted ratio is formally a lower limit. Conversely, magnetic fields as low as $\sim$1/3 of our quoted values are strictly allowed if we invoke a sharper cutoff in the synchrotron spectrum at $\gtrsim 60$ GHz, as would be expected in some aging models for extended radio lobes (cf., (*9*)). Such models with lower magnetic fields and EEDs with sharper upper energy cutoffs than the exponential form adopted here (Fig. 3) would result in IC spectra where the EBL rather than the CMB component become dominant in the LAT observing band. These models require large departures from equipartition ($U_{\rm e}/U_{\rm B} \gtrsim 10$); even lower B-fields would violate the observed X-ray limit to the lobe flux (*9*, *23*).

For a tangled magnetic field, the total non-thermal pressures in the lobes are, $p_{\rm rel} = (U_{\rm e} + U_{\rm B})/3 \simeq 5.6 \times 10^{-14}$ erg cm^{-3} (north) and $\simeq 2.7 \times 10^{-14}$ erg cm^{-3} (south). Such estimates can be compared to the ambient thermal gas pressure to enable further understanding of the dynamical evolution of such giant structures in general. Unfortunately, the parameters of the thermal gas at the appropriate distances from the nucleus of Cen A are not well known. Upper limits of the soft X-ray emission of the lobes (*9*), as well as Faraday rotation studies (*24*) indicate that the thermal gas number density is $n_{\rm gas} < 10^{-4}$ cm^{-3} within the giant lobes. Hence, the upper limit for the thermal pressure, $p_{\rm gas} = nkT < 10^{-13}\,(n_{\rm gas}/10^{-4}\,{\rm cm}^{-3})\,(T_{\rm gas}/10^{7}\,{\rm K})$ erg cm^{-3}, is comparable to the evaluated non-thermal pressures.

Our modeling results allow us to estimate the total energy in both giant lobes, $E_{\rm tot} \simeq 1.5 \times 10^{58}$ erg. This, divided by the lifetime of the lobes derived from spectral aging (*9*), $\tau \simeq 3 \times 10^{7}$ yrs, gives the required kinetic power of the jets inflating the giant lobes, $L_{\rm j} \simeq E_{\rm tot}/2\,\tau \simeq 7.7 \times 10^{42}$ erg s^{-1}, which is close to the estimates of the total power of the kpc-scale outflow in the current epoch of jet activity (*25*). For a black hole mass in Cen A, $M_{\rm BH} \simeq 10^{8}\,M_{\odot}$ (*26*),

this implies a jet power which is only a small fraction of the Eddington luminosity ($L_{\rm j} \simeq 6.1 \times 10^{-4} L_{\rm Edd}$), and a relatively small jet production efficiency, $E_{\rm tot}/M_{\rm BH}c^2 \simeq 8 \times 10^{-5}$. Because the $p\,dV$ work done by the expanding lobes on the ambient medium is not taken into account, and the relativistic proton content is unconstrained in our analysis, the obtained values for $E_{\rm tot}$ and $L_{\rm j}$ are strict lower limits and could plausibly be an order of magnitude larger (cf., (*27*)).

The observed LAT emission implies the presence of 0.1–1 TeV electrons in the > 100's kpc-scale lobes. Because their radiative lifetimes ($<$ 1–10 Myr) approach plausible electron transport timescales across the lobes, the particles have either been accelerated in situ or efficiently transported from regions closer to the nucleus. Such high-energy electrons in the lobes are in fact required to IC scatter photons into the LAT band and it is presently unclear how common this is in other radio galaxies.

References and Notes

1. J. G. Bolton, G. J. Stanley, O. B. Slee, *Nature* **164**, 101 (1949).

2. C. A. Shain, *Aust. J. Phys.* **11**, 517 (1958).

3. K. V. Sheridan, *Aust. J. Phys.* **11**, 400 (1958).

4. L. Ferrarese *et al.*, *Astrophys. J.* **654**, 186 (2007).

5. W. B. Atwood *et al.* ($Fermi$-LAT collaboration), *Astrophys. J.* **697**, 1071 (2009).

6. R. C. Hartman *et al.*, *Astrophys. J. Suppl. Ser.* **123**, 79 (1999).

7. http://fermi.gsfc.nasa.gov/ssc/data/analysis/documentation/Cicerone/

8. G. Hinshaw *et al.*, *Astrophys. J. Suppl. Ser.* **180**, 225 (2009).

9. M. J. Hardcastle, C. C. Cheung, I. J. Feain, Ł. Stawarz, *Mon. Not. R. Astron. Soc.* **393**, 1041 (2009).

10. J. R. Mattox *et al.*, *Astrophys. J.* **461**, 396 (1996).

11. D. E. Harris, J. E. Grindlay, *Mon. Not. R. Astron. Soc.* **188**, 25 (1979).

12. E. D. Feigelson *et al.*, *Astrophys. J. Lett.* **449**, L149 (1995).

13. J. H. Croston *et al.*, *Astrophys. J.* **626**, 733 (2005).

14. J. Kataoka, Ł. Stawarz, *Astrophys. J.* **622**, 797 (2005).

15. C. C. Cheung, *AIP Conf. Ser.* **921**, 325 (2007).

16. N. Junkes, R. F. Haynes, J. I. Harnett, D. L. Jauncey, *Astron. Astrophys.* **269**, 29 (1993).

17. H. Alvarez, J. Aparici, J. May, P. Reich, *Astron. Astrophys.* **355**, 863 (2000).

18. A. Crusius, R. Schlickeiser, *Astron. Astrophys.* **164**, L16 (1986).

19. G. R. Blumenthal, R. J. Gould, *Rev. Mod. Phys.* **42**, 237 (1970).

20. M. G. Hauser, E. Dwek, *Annu. Rev. Astron. Astrophys.* **39**, 249 (2001).

21. M. Georganopoulos *et al.*, *Astrophys. J. Lett.* **686**, L5 (2008).

22. M. Raue, D. Mazin, *Int. J. Mod. Phys. D* **17**, 1515 (2008).

23. F. J. Marshall, G. W. Clark, *Astrophys. J.* **245**, 840 (1981).

24. I. J. Feain *et al.*, *Astrophys. J.* **707**, 114 (2009).

25. J. H. Croston *et al.*, *Mon. Not. R. Astron. Soc.* **395**, 1999 (2009).

26. A. Marconi *et al.*, *Astron. Astrophys.* **448**, 921 (2006).

27. C. D. Dermer, S. Razzaque, J. D. Finke, A. Atoyan, *New J. Phys.* **11**, 065016 (2009).

28. The $Fermi$ LAT Collaboration acknowledges support from a number of agencies and institutes for both development and the operation of the LAT as well as scientific data analysis. These include NASA and DOE in the United States, CEA/Irfu and IN2P3/CNRS in France, ASI and INFN in Italy, MEXT, KEK, and JAXA in Japan, and the K. A. Wallenberg Foundation, the Swedish Research Council and the National Space Board in Sweden. Additional support from INAF in Italy and CNES in France for science analysis during the operations phase is also gratefully acknowledged. C.C.C. was supported by the NASA Postdoctoral Program at GSFC, administered by ORAU through a contract with NASA. We thank N. Odegard for providing the WMAP image.

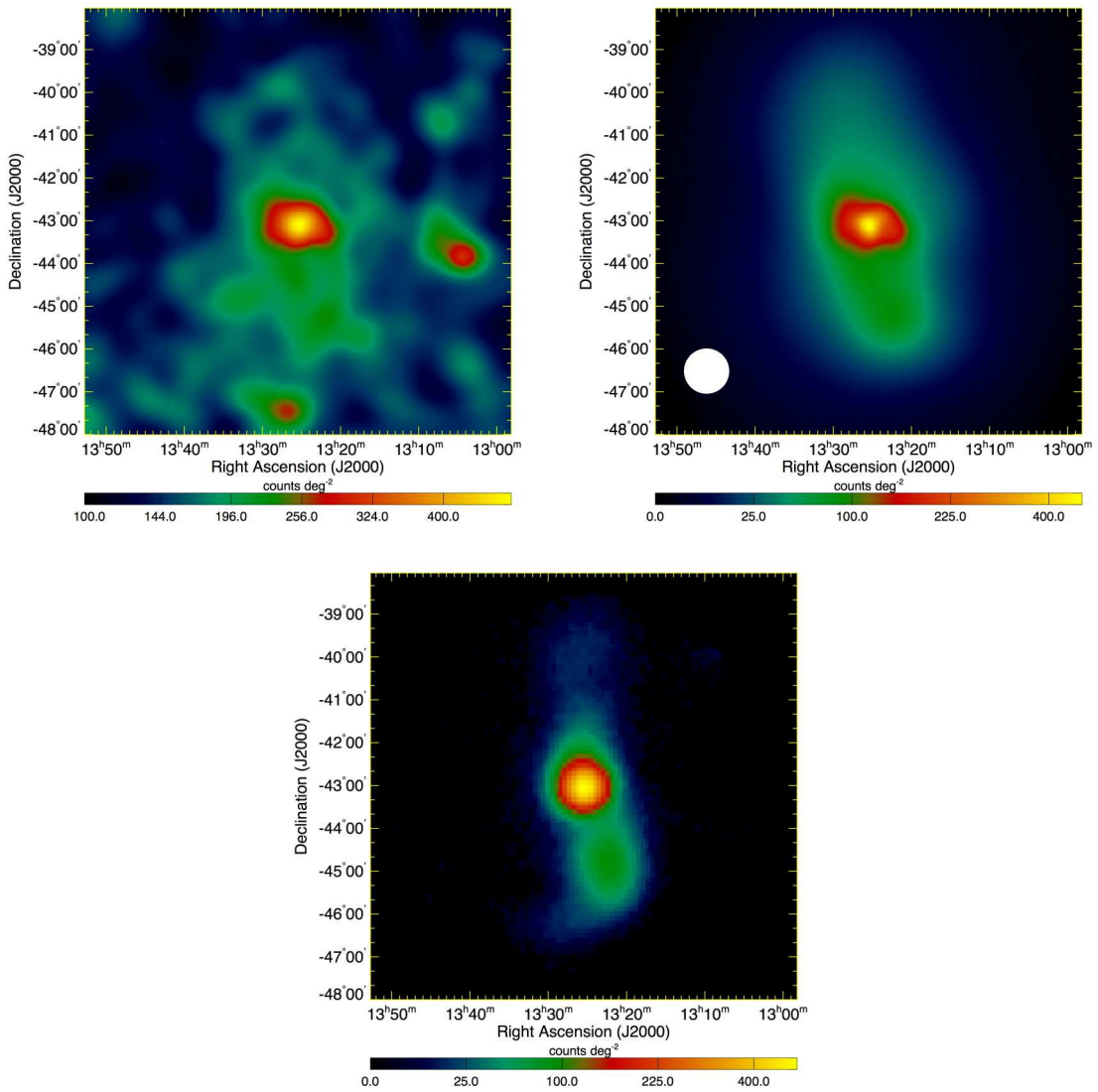

Fig. 1. $Fermi$-LAT γ-ray ($>$200 MeV) counts maps centered on Cen A displayed with square-root scaling **(A, B)**. In both panels, a model of the Galactic and isotropic emission components were subtracted (in contrast to the observed counts profile presented in Fig. 2). The images are shown before **(A)** and and after **(B)** additional subtraction of field point sources (SOM), and are shown adaptively smoothed with a minimum signal-to-noise ratio of 10. In panel **(B)**, the white circle with a diameter of 1° is approximately the scale of the LAT PSF width. For comparison, the 22 GHz radio map from the 5-year WMAP dataset (*8*) with a resolution 0°.83 is shown **(C)**.

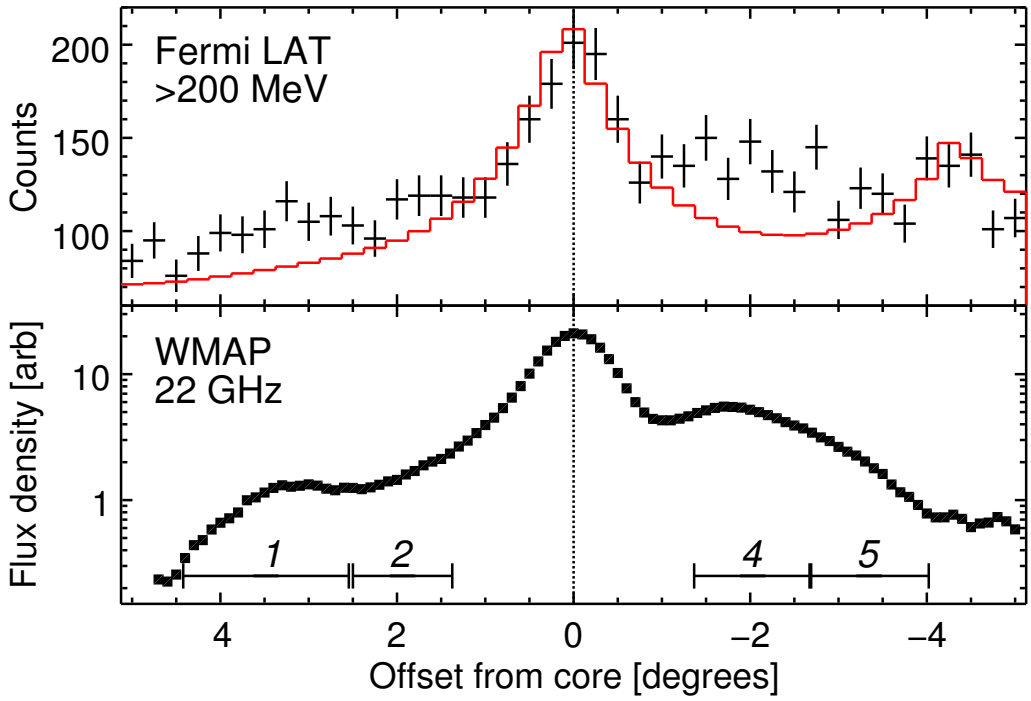

Fig. 2. Observed intensity profiles of Cen A along the north-south axis in γ-rays [top panel] and radio [bottom panel]. In the bottom panel, the lobe regions 1 & 2 (northern lobe), and 4 & 5 (southern lobe) are indicated following (9) where region 3 (not indicated) is the core. The red curve overlaid onto the LAT data indicates the emission model for of all fitted points sources plus the isotropic and Galactic diffuse (brighter to the south) emission. The point sources include the Cen A core (offset=0°) and a LAT source at an offset=−4.5° (see SOM) which is clearly outside (1° from the southern edge) of the southern lobe. The excess counts are coincident with the northern and southern giant lobes.

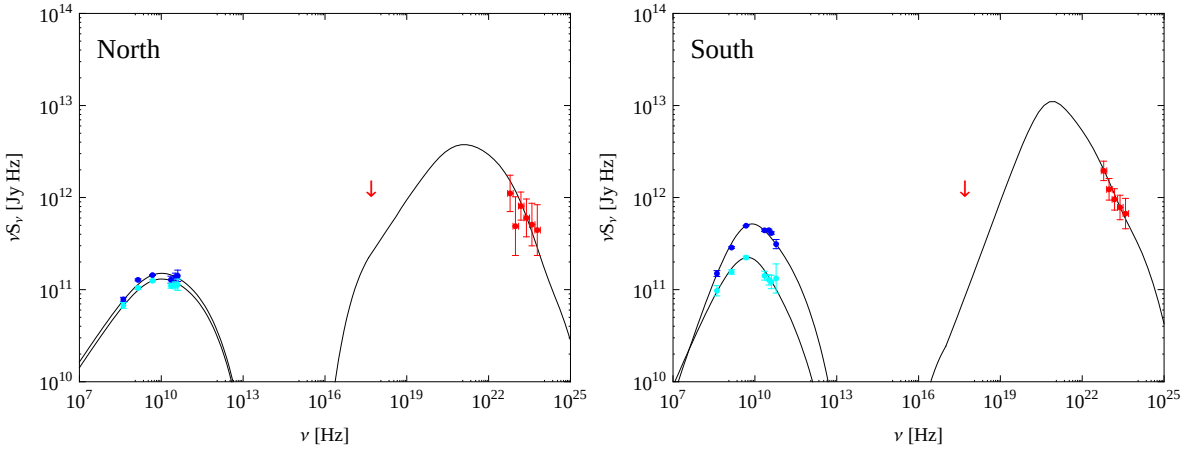

Fig. 3. Broad-band spectral energy distributions (SEDs) of the northern **(A)** and southern **(B)** giant lobes of Cen A. The radio measurements (up to 60 GHz) of each lobe are separated into 2 regions with blue data points indicating regions (2 and 4; cf., Fig. 2) closer to the nucleus and the farther regions (1 and 5) in light blue. Synchrotron continuum models for each region are overlaid (see text). The component at higher energies is the total IC emission of each lobe modeled to match the LAT measurements (red points with error bars). The X-ray limit for the lobe emission derived from SAS-3 observations (*23*) is indicated with a red arrow; see (*9*). The break and maximum frequencies in the synchrotron spectra are $\nu_{\rm br} = 4.8$ GHz and $\nu_{\rm max} = 400$ GHz, respectively.

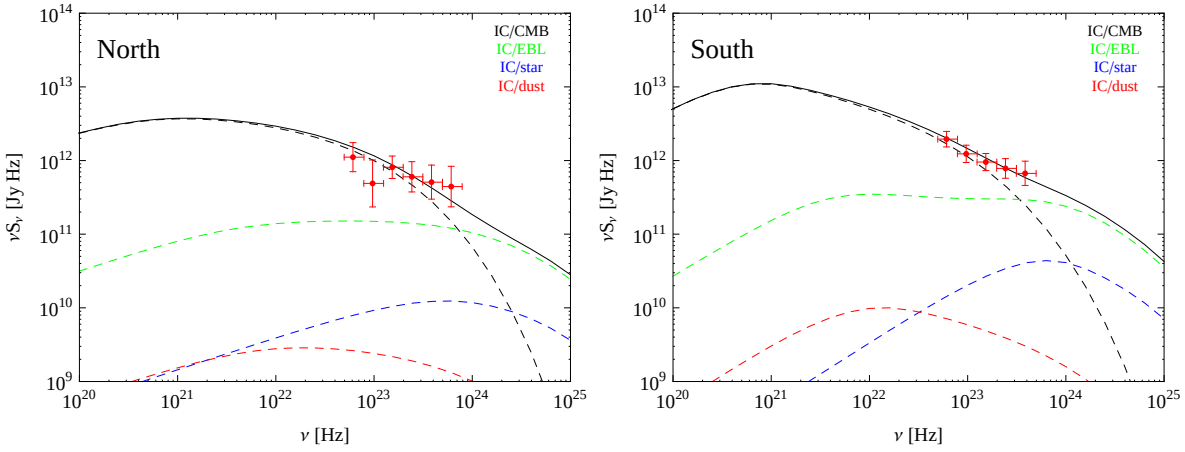

Fig. 4. Detail of the IC portion of the northern **(A)** and southern **(B)** giant lobes' SEDs (cf., Fig. 3). The separate contributions from the different photon seed sources are indicated with dashed lines while the total emission is the solid black line.

The Fermi LAT Collaboration

A. A. Abdo[1,2], M. Ackermann[3], M. Ajello[3], W. B. Atwood[4], L. Baldini[5], J. Ballet[6], G. Barbiellini[7,8], D. Bastieri[9,10], B. M. Baughman[11], K. Bechtol[3], R. Bellazzini[5], B. Berenji[3], R. D. Blandford[3], E. D. Bloom[3], E. Bonamente[12,13], A. W. Borgland[3], J. Bregeon[5], A. Brez[5], M. Brigida[14,15], P. Bruel[16], T. H. Burnett[17], S. Buson[10], G. A. Caliandro[18], R. A. Cameron[3], P. A. Caraveo[19], J. M. Casandjian[6], E. Cavazzuti[20], C. Cecchi[12,13], Ö. Çelik[21,22,23], A. Chekhtman[1,24], C. C. Cheung[1,2,21*], J. Chiang[3], S. Ciprini[13], R. Claus[3], J. Cohen-Tanugi[25], S. Colafrancesco[20], L. R. Cominsky[26], J. Conrad[27,28,29], L. Costamante[3], S. Cutini[20], D. S. Davis[21,23], C. D. Dermer[1], A. de Angelis[30], F. de Palma[14,15], S. W. Digel[3], E. do Couto e Silva[3], P. S. Drell[3], R. Dubois[3], D. Dumora[31,32], C. Farnier[25], C. Favuzzi[14,15], S. J. Fegan[16], J. Finke[1,2], W. B. Focke[3], P. Fortin[16], Y. Fukazawa[33*], S. Funk[3], P. Fusco[14,15], F. Gargano[15], D. Gasparrini[20], N. Gehrels[21,34,35], M. Georganopoulos[23], S. Germani[12,13], B. Giebels[16], N. Giglietto[14,15], F. Giordano[14,15], M. Giroletti[36], T. Glanzman[3], G. Godfrey[3], I. A. Grenier[6], J. E. Grove[1], L. Guillemot[37], S. Guiriec[38], Y. Hanabata[33], A. K. Harding[21], M. Hayashida[3], E. Hays[21], R. E. Hughes[11], M. S. Jackson[28,39], G. Jóhannesson[3], A. S. Johnson[3], T. J. Johnson[21,35], W. N. Johnson[1], T. Kamae[3], H. Katagiri[33], J. Kataoka[40], N. Kawai[41,42], M. Kerr[17], J. Knödlseder[43*], M. L. Kocian[3], M. Kuss[5], J. Lande[3], L. Latronico[5], M. Lemoine-Goumard[31,32], F. Longo[7,8], F. Loparco[14,15], B. Lott[31,32], M. N. Lovellette[1], P. Lubrano[12,13], G. M. Madejski[3], A. Makeev[1,24], M. N. Mazziotta[15], W. McConville[21,35], J. E. McEnery[21,35], C. Meurer[27,28], P. F. Michelson[3], W. Mitthumsiri[3], T. Mizuno[33], A. A. Moiseev[22,35], C. Monte[14,15], M. E. Monzani[3], A. Morselli[44], I. V. Moskalenko[3], S. Murgia[3], P. L. Nolan[3], J. P. Norris[45], E. Nuss[25], T. Ohsugi[33], N. Omodei[5], E. Orlando[46], J. F. Ormes[45], D. Paneque[3], D. Parent[31,32], V. Pelassa[25], M. Pepe[12,13], M. Pesce-Rollins[5], F. Piron[25], T. A. Porter[4], S. Rainò[14,15], R. Rando[9,10], M. Razzano[5], S. Razzaque[1,2], A. Reimer[47,3], O. Reimer[47,3], T. Reposeur[31,32], S. Ritz[4], L. S. Rochester[3], A. Y. Rodriguez[18], R. W. Romani[3], M. Roth[17], F. Ryde[39,28], H. F.-W. Sadrozinski[4], R. Sambruna[21], D. Sanchez[16], A. Sander[11], P. M. Saz Parkinson[4], J. D. Scargle[48], C. Sgrò[5], E. J. Siskind[49],

D. A. Smith[31,32], P. D. Smith[11], G. Spandre[5], P. Spinelli[14,15], J.-L. Starck[6], Ł. Stawarz[50,3*], M. S. Strickman[1], D. J. Suson[51], H. Tajima[3], H. Takahashi[33], T. Takahashi[52], T. Tanaka[3], J. B. Thayer[3], J. G. Thayer[3], D. J. Thompson[21], L. Tibaldo[9,10,6], D. F. Torres[53,18], G. Tosti[12,13], A. Tramacere[3,54], Y. Uchiyama[3], T. L. Usher[3], V. Vasileiou[22,23], N. Vilchez[43], V. Vitale[44,55], A. P. Waite[3], E. Wallace[17], P. Wang[3], B. L. Winer[11], K. S. Wood[1], T. Ylinen[39,56,28], M. Ziegler[4], M. J. Hardcastle[57], D. Kazanas[21]

1. Space Science Division, Naval Research Laboratory, Washington, DC 20375, USA

2. National Research Council Research Associate, National Academy of Sciences, Washington, DC 20001, USA

3. W. W. Hansen Experimental Physics Laboratory, Kavli Institute for Particle Astrophysics and Cosmology, Department of Physics and SLAC National Accelerator Laboratory, Stanford University, Stanford, CA 94305, USA

4. Santa Cruz Institute for Particle Physics, Department of Physics and Department of Astronomy and Astrophysics, University of California at Santa Cruz, Santa Cruz, CA 95064, USA

5. Istituto Nazionale di Fisica Nucleare, Sezione di Pisa, I-56127 Pisa, Italy

6. Laboratoire AIM, CEA-IRFU/CNRS/Université Paris Diderot, Service d'Astrophysique, CEA Saclay, 91191 Gif sur Yvette, France

7. Istituto Nazionale di Fisica Nucleare, Sezione di Trieste, I-34127 Trieste, Italy

8. Dipartimento di Fisica, Università di Trieste, I-34127 Trieste, Italy

9. Istituto Nazionale di Fisica Nucleare, Sezione di Padova, I-35131 Padova, Italy

10. Dipartimento di Fisica “G. Galilei”, Università di Padova, I-35131 Padova, Italy

11. Department of Physics, Center for Cosmology and Astro-Particle Physics, The Ohio State University, Columbus, OH 43210, USA

12. Istituto Nazionale di Fisica Nucleare, Sezione di Perugia, I-06123 Perugia, Italy

13. Dipartimento di Fisica, Università degli Studi di Perugia, I-06123 Perugia, Italy

14. Dipartimento di Fisica “M. Merlin” dell’Università e del Politecnico di Bari, I-70126 Bari, Italy

15. Istituto Nazionale di Fisica Nucleare, Sezione di Bari, 70126 Bari, Italy

16. Laboratoire Leprince-Ringuet, École polytechnique, CNRS/IN2P3, Palaiseau, France

17. Department of Physics, University of Washington, Seattle, WA 98195-1560, USA

18. Institut de Ciencies de l’Espai (IEEC-CSIC), Campus UAB, 08193 Barcelona, Spain

19. INAF-Istituto di Astrofisica Spaziale e Fisica Cosmica, I-20133 Milano, Italy

20. Agenzia Spaziale Italiana (ASI) Science Data Center, I-00044 Frascati (Roma), Italy

21. NASA Goddard Space Flight Center, Greenbelt, MD 20771, USA

22. Center for Research and Exploration in Space Science and Technology (CRESST) and NASA Goddard Space Flight Center, Greenbelt, MD 20771, USA

23. Department of Physics and Center for Space Sciences and Technology, University of Maryland Baltimore County, Baltimore, MD 21250, USA

24. George Mason University, Fairfax, VA 22030, USA

25. Laboratoire de Physique Théorique et Astroparticules, Université Montpellier 2, CNRS/IN2P3, Montpellier, France

26. Department of Physics and Astronomy, Sonoma State University, Rohnert Park, CA 94928-3609, USA

27. Department of Physics, Stockholm University, AlbaNova, SE-106 91 Stockholm, Sweden

28. The Oskar Klein Centre for Cosmoparticle Physics, AlbaNova, SE-106 91 Stockholm, Sweden

29. Royal Swedish Academy of Sciences Research Fellow, funded by a grant from the K. A. Wallenberg Foundation

30. Dipartimento di Fisica, Università di Udine and Istituto Nazionale di Fisica Nucleare, Sezione di Trieste, Gruppo Collegato di Udine, I-33100 Udine, Italy

31. Université de Bordeaux, Centre d'Études Nucléaires Bordeaux Gradignan, UMR 5797, Gradignan, 33175, France

32. CNRS/IN2P3, Centre d'Études Nucléaires Bordeaux Gradignan, UMR 5797, Gradignan, 33175, France

33. Department of Physical Sciences, Hiroshima University, Higashi-Hiroshima, Hiroshima 739-8526, Japan

34. Department of Astronomy and Astrophysics, Pennsylvania State University, University Park, PA 16802, USA

35. Department of Physics and Department of Astronomy, University of Maryland, College Park, MD 20742, USA

36. INAF Istituto di Radioastronomia, 40129 Bologna, Italy

37. Max-Planck-Institut für Radioastronomie, Auf dem Hügel 69, 53121 Bonn, Germany

38. Center for Space Plasma and Aeronomic Research (CSPAR), University of Alabama in Huntsville, Huntsville, AL 35899, USA

39. Department of Physics, Royal Institute of Technology (KTH), AlbaNova, SE-106 91 Stockholm, Sweden

40. Waseda University, 1-104 Totsukamachi, Shinjuku-ku, Tokyo, 169-8050, Japan

41. Department of Physics, Tokyo Institute of Technology, Meguro City, Tokyo 152-8551, Japan

42. Cosmic Radiation Laboratory, Institute of Physical and Chemical Research (RIKEN), Wako, Saitama 351-0198, Japan

43. Centre d'Étude Spatiale des Rayonnements, CNRS/UPS, BP 44346, F-30128 Toulouse Cedex 4, France

44. Istituto Nazionale di Fisica Nucleare, Sezione di Roma "Tor Vergata", I-00133 Roma, Italy

45. Department of Physics and Astronomy, University of Denver, Denver, CO 80208, USA

46. Max-Planck Institut für extraterrestrische Physik, 85748 Garching, Germany

47. Institut für Astro- und Teilchenphysik and Institut für Theoretische Physik, Leopold-Franzens-Universität Innsbruck, A-6020 Innsbruck, Austria

48. Space Sciences Division, NASA Ames Research Center, Moffett Field, CA 94035-1000, USA

49. NYCB Real-Time Computing Inc., Lattingtown, NY 11560-1025, USA

50. Astronomical Observatory, Jagiellonian University, 30-244 Kraków, Poland

51. Department of Chemistry and Physics, Purdue University Calumet, Hammond, IN 46323-2094, USA

52. Institute of Space and Astronautical Science, JAXA, 3-1-1 Yoshinodai, Sagamihara, Kanagawa 229-8510, Japan

53. Institució Catalana de Recerca i Estudis Avançats (ICREA), Barcelona, Spain

54. Consorzio Interuniversitario per la Fisica Spaziale (CIFS), I-10133 Torino, Italy

55. Dipartimento di Fisica, Università di Roma "Tor Vergata", I-00133 Roma, Italy

56. School of Pure and Applied Natural Sciences, University of Kalmar, SE-391 82 Kalmar, Sweden

57. Centre for Astrophysics Research, University of Hertfordshire, College Lane, Hatfield AL10 9AB, UK

† To whom correspondence should be addressed.
E-mail: Teddy.Cheung.ctr@nrl.navy.mil (C.C.C.); fukazawa@hep01.hepl.hiroshima-u.ac.jp (Y.F.); jurgen.knodlseder@cesr.fr (J.K.); stawarz@slac.stanford.edu (Ł.S.)

Supporting Online Material (SOM)

Materials and Methods: LAT Data Selection and Tests of Spatial Modeling

The characteristics and performance of the LAT aboard *Fermi* are described in detail by (*S1*). The data used in this work amount to 300 days of continuous sky survey observations over the period August 4th 2008 – May 31st 2009 (corresponding to mission elapsed times (MET) 239557420 - 265507200) during which an effective exposure of $\sim 2.3 \times 10^{10}$ cm^2 s (at 1 GeV) is obtained for Cen A. Events satisfying the standard low-background event selection ("Pass 6 Diffuse" events) (*S1*), coming from zenith angles $< 105^\circ$ and satisfying the rocking angle cut of 39° are used (*S2*). We further restrict the analysis to photon energies above 200 MeV; below this energy the effective area in the Diffuse class is relatively small and strongly dependent on energy.

For the analysis we select all events within a rectangular region-of-interest (ROI) of size $14^\circ \times 14^\circ$ centered on $(\alpha_{\rm J2000}, \delta_{\rm J2000}) = (13^{\rm h}25^{\rm m}26^{\rm s}, -43^\circ 01' 12")$ and aligned in equatorial coordinates. A counts map of the ROI is shown in Fig. S1. All analysis is performed using the LAT Science Tools package, which is available from the Fermi Science Support Center (*S3*), using P6_V3 post-launch instrument response functions (IRFs). These take into account pile-up and accidental coincidence effects in the detector subsystems that were not considered in the definition of the pre-launch IRFs. At the Galactic latitude of Cen A ($b \approx +19^\circ$), the γ-ray background is a combination of extragalactic and Galactic diffuse emissions and some residual instrumental background. We model the Galactic background component using the LAT standard diffuse background model `gll_iem_v02`[1] for which we keep the overall normalization as a free parameter. The extragalactic and residual instrumental backgrounds are combined into

[1]The model can be downloaded from http://fermi.gsfc.nasa.gov/ssc/data/access/lat/BackgroundModels.html.

a single component which has been taken as being isotropic and with a spectral distribution determined from all-sky fitting (file `isotropic_iem_v02.txt`). The normalization of this component was left as a free parameter.

The first *Fermi*-LAT source catalog (*S4*) contains 14 point sources within the ROI. One of these sources (1FGL J1325.6−4300) corresponds to the core of Cen A while two sources (1FGL J1322.0−4515, 1FGL J1333.4−4036) are likely local maxima of the Cen A lobes. This leaves 11 point sources within the ROI that are not associated to Cen A. To correctly account for these 11 field sources in our analysis, we include point sources at the positions quoted in Table S2 in our background model for which we left the fluxes and spectral power-law indices as free parameters. The locations of the point sources are indicated by boxes in Fig. S1.

We model the core emission from Cen A with a point source located at the known radio position of $(\alpha_{\rm J2000}, \delta_{\rm J2000}) = (13^{\rm h}25^{\rm m}27^{\rm s}, -43°01'09")$ for which we keep the flux and power-law spectral index as free parameters. The giant radio lobes of Cen A are modeled using a spatial template that is based on the WMAP 22 GHz image (*S5*) of Cen A (see main text and Fig. S1). To exclude the core emission from this template we set all pixels within a radius of $1°$ around the core of Cen A to zero. We further split the template along an east-west axis running through the core of Cen A to obtained separate models for the northern and southern radio lobes. We model the spectrum of both lobes using power laws for which we keep the fluxes and spectral indices as free parameters.

We fit the core and radio lobes in addition to the background model to the data using a binned maximum likelihood optimization. The test statistic (TS) (*S6*) of the core amounts to 219, corresponding to a detection significance of 14.6σ. For the northern and southern lobes we obtain TS values of 29 and 69, which corresponds to detection significances of 5.0σ and 8.0σ, respectively. As a test, fake WMAP image templates were created by rotating the map by $90°$, $180°$, and $270°$, bringing the lobes out of the alignment with respect to the radio emission. As

expected, when fitting the data with these fake maps instead of the original WMAP template the TS is reduced by a large factor (~ 4), indicating that the γ-ray emission indeed matches the radio morphology.

As Cen A is relatively close to the Galactic plane, an accurate modeling of the diffuse Galactic emission is important. We tested the stability of our results by replacing the standard model of diffuse Galactic emission by the model `gll_iem_v01`, i.e., from the GALPROP code (*S2*) and this is considered as a source of systematic uncertainty. The effect of different core exclusion radii was also tested, considering values of 1.5° and 1.25° in addition to the 1° results quoted. The lower end of this range is defined by excluding enough of the core to sufficiently model its emission, and the upper end is the radius in which the lobe emission begins to be excluded. Lastly, systematic uncertainties were calculated considering the effect of the uncertainty in the IRFs (i.e., the LAT effective area, $A_{\rm eff}$). These are summarized in Table S3.

To investigate whether the γ-ray emission seen towards the giant radio lobes of Cen A could also be attributed to background blazars in the area, we have shown in the right panel of Fig. S1 the distribution of blazar candidates in the CRATES catalog of flat-spectrum radio sources (*S7*) within the ROI. We found a total of 11 γ-ray blazar candidates that spatially overlap with the radio lobes of Cen A. From Fig. S1 we can already notice that none of them coincides with a local maximum of γ-ray emission in the counts map. Fitting point sources at the positions of the 11 CRATES sources with flux and spectral power law index set free in addition to the core and lobe model of Cen A does not result in a significant detection for any of them, and does not lead to a significant reduction of the flux from the WMAP template that models the γ-ray emission from the lobes. We thus conclude that the emission seen towards the Cen A radio lobes cannot be attributed to known blazars in the field. Extended emission from the giant radio lobes of Cen A seems thus as the most plausible explanation of the observations.

Theoretical Modeling

Following (*S8*), we used a template elliptical galaxy spectrum (*S9*) normalized to the V-band apparent magnitude, $m_V = 7.0$ (*S10*) to derive a luminosity of the host of $L_V \simeq 7.8 \times 10^{43}$ erg s^{-1} in this band. The far-infrared (FIR) emission of the dust lane is modeled as a modified blackbody, $\nu I_\nu(T_{\rm d}) \propto \nu^4 \, (1 - \exp[-(\nu/\nu_0)^{-\beta}])/(\exp[h\nu/kT_d] - 1)$, where $\beta = 1.5$ is the dust emissivity power-law, $T_{\rm d} \simeq 60\,$K is the assumed dust temperature (corresponding to the peak frequencies, $\nu_{\rm d} = 3kT_{\rm d}/h \simeq 3.75 \times 10^{12}\,$Hz), and $\nu_0 = 3 \times 10^{12}\,$Hz is the frequency below which the thermal dust emission becomes optically thin. This distribution is normalized to the total $100\,\mu$m Cen A flux of $400\,$Jy (*S11*), amounting to a luminosity of $L_{100} \simeq 2 \times 10^{43}$ erg s^{-1} at this wavelength. The spectra generated in this way are consistent with the monochromatic flux density measurements compiled by (*S12*).

In Fig. S2, the relevant photon fields as seen by the lobes are plotted. These include the CMB (black) and the solid green line denotes the EBL model from (*S13*) adopted in our calculations (see main text); green dashed lines are the other EBL models considered (see Fig. S3). The volume averaged energy density of the starlight (blue) and dust (red) emission as seen at the locations of regions 1 and 2 (lower and upper solid, respectively) and 4 and 5 (upper and lower dashed, respectively) are indicated. For all EBL choices, the EBL energy density dominates over that of the host galaxy starlight and dust emission by $\gtrsim$ 3–100$\times$. Here, the lobes are assumed to lie in the plane of the sky. This assumption maximizes the possible contribution of the galactic emission as smaller angles to the line of sight result in larger de-projected distances for the radio lobes and would make the galactic photon fields even less relevant. In terms of our modeling results, smaller angles would also imply larger source volumes which would affect only the jet powers evaluated (making them larger), so the quoted estimate should further be considered as a lower limit.

As mentioned in the main text, we parameterize the electron energy distribution (EED) of each lobe region with a broken power-law in the form: $n_{\rm e}(\gamma) = k_{\rm e}\,\gamma^{-s_1}$ for $\gamma_{\rm min} \leq \gamma < \gamma_{\rm br}$ and $n_{\rm e}(\gamma) = k_{\rm e}\,\gamma_{\rm br}^{s_2-s_1}\,\gamma^{-s_2}\,\exp[-\gamma/\gamma_{\rm max}]$ for $\gamma \geq \gamma_{\rm br}$. We initially considered a wide range of magnetic field strengths, $B = 0.1 - 10\mu$G, and adjusted the parameters of the EED ($k_{\rm e}$, s_1, s_2, $\gamma_{\rm br}$, and $\gamma_{\rm max}$) to match the radio measurements. The IC fluxes were evaluated separately for each defined region (1, 2, 4, and 5) and the summed computed emission from each lobe was compared to the observed LAT spectra. The models found to best represent the radio and γ-ray measurements are reported (Table S1). Using different EBL models/compilations (Fig. S3), we found the resultant IC SEDs are insensitive to the particular EBL models within the measurement uncertainties.

The low-energy ultrarelativistic electron energy distributions in the south lobe are relatively flat, with indices $s_1 < 2$. We note in this context that since the synchrotron continua for this lobe are significantly curved, the precise synchrotron kernel has to be used in evaluating the synchrotron emission for a given form of the electron spectrum. That is, no standard approximation relating the synchrotron spectral index, α (defined as $S_\nu \propto \nu^{-\alpha}$), with the electron energy index, $s = 2\alpha + 1$, can be made. Such an approximation holds when the electron energy distribution is of the form of a single (and steep) power-law, but not if the electron spectrum has a sharp break, which – in the considered case – affects the synchrotron spectra in the GHz range for the Cen A south lobe. If we increase s_1 for the southern lobe up to 2, we would not be able to reproduce the radio data well. We also note that with $s_1 < 2$, the derived total electron energy density ($U_{\rm e}$) of the southern lobe is relatively insensitive to our assumption of the minimum electron energy ($\gamma_{\rm min} = 1$) with a decrease by only a few percent if we increase $\gamma_{\rm min}$ to 100 for example. For the north lobe however, increasing $\gamma_{\rm min}$ to 100 would result in a non-negligible ($\simeq 2\times$) decrease in $U_{\rm e}$ because this lobe is characterized by a steeper low-energy electron spectrum.

In addition to the galactic emission, one can expect that the non-thermal emission from the active nucleus also illuminates the giant lobes, thus providing another possible seed photon source. For Cen A, the energy density of the nuclear emission at a distance $r \sim 100$ kpc from the nucleus (corresponding to regions 2 and 4) can be estimated roughly as, $U_{\rm nuc} \lesssim 10^{-14}$ erg cm^{-3} (see (*S14*)). This is comparable at best to the EBL level at near-infrared/optical wavelengths but as the precise level is dependent on the unknown relativistic beaming parameters of the inner jet and uncertainty in the jet duty cycle, this is omitted in our estimates for simplicity.

References and Notes

S1. W. B. Atwood *et al.* ($Fermi$-LAT collaboration), *Astrophys. J.* **697**, 1071 (2009).

S2. A. A. Abdo *et al.* ($Fermi$-LAT collaboration), *Astrophys. J. Suppl. Ser.* **183**, 46 (2009).

S3. http://fermi.gsfc.nasa.gov/ssc/data/analysis/documentation/Cicerone/

S4. A. A. Abdo *et al.* ($Fermi$-LAT collaboration), *Astrophys. J. Suppl. Ser.*, submitted, arXiv/1002.2280v1 (2010).

S5. G. Hinshaw *et al.*, *Astrophys. J. Suppl. Ser.* **180**, 225 (2009).

S6. J. R. Mattox *et al.*, *Astrophys. J.* **461**, 396 (1996).

S7. S. E. Healey *et al.*, *Astrophys. J. Suppl. Ser.* **171**, 61 (2007).

S8. Ł. Stawarz, F. Aharonian, S. Wagner, M. Ostrowski, *Mon. Not. R. Astron. Soc.* **371**, 1705 (2006).

S9. L. Silva, G. L. Granato, A. Bressan, L. Danese, *Astrophys. J.* **509**, 103 (1998).

S10. F. P. Israel, *Astron. Astrophys. Rev.* **8**, 237 (1998).

S11. D. Golombek, G. K. Miley, G. Neugebauer, *Astron. J.* **95**, 26 (1988).

S12. J. H. Croston *et al.*, *Mon. Not. R. Astron. Soc.* **395**, 1999 (2009).

S13. M. Raue, D. Mazin, *Int. J. Mod. Phys. D* **17**, 1515 (2008).

S14. Ł. Stawarz, M. Sikora, M. Ostrowski, *Astrophys. J.* **597**, 186 (2003).

S15. J. D. Finke, S. Razzaque, C. D. Dermer, *Astrophys. J.*, in press, arXiv:0905.1115v2 (2010).

S16. A. Franceschini, G. Rodighiero, M. Vaccari, *Astron. Astrophys.* **487**, 837 (2008).

S17. R. C. Gilmore, P. Madau, J. R. Primack, R. S. Somerville, *AIP Conf. Ser.* **1085**, 577 (2008).

S18. T. M. Kneiske, T. Bretz, K. Mannheim, D. H. Hartmann, *Astron. Astrophys.* **413**, 807 (2004).

S19. F. W. Stecker, M. A. Malkan, S. T. Scully, *Astrophys. J.* **648**, 774 (2006).

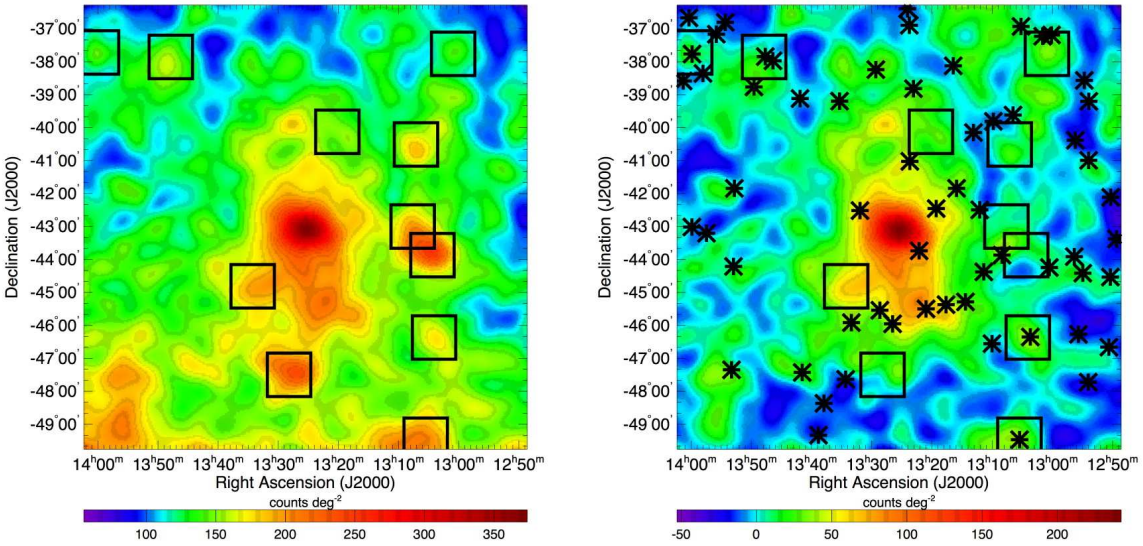

Fig. S1. Gaussian kernel ($\sigma = 0.3^\circ$) smoothed counts maps of the region-of-interest (ROI) around Cen A in a true local projection before (left) and after subtraction of the background model (right) for the energy range 200 MeV – 30 GeV and for a pixel size of $0.1^\circ \times 0.1^\circ$. The boxes show the locations of the 11 LAT point sources that have been included in the background model. The stars in the right panel show the locations of the CRATES radio sources in the ROI.

	North		South	
Region	1	2	4	5
Distance from core [kpc]	226	125	131	217
Cylindrical dimensions (L, r) [kpc]	$(122, 81)$	$(73, 70.5)$	$(86, 78)$	$(87, 69.5)$
F(>100 MeV) [10^{-7} ph cm^{-2} s^{-1}]	0.77 (+0.23/–0.19)		1.09 (+0.24/–0.21)	
Photon index	2.52 (+0.16/–0.19)		2.60 (+0.14/–0.15)	
$k_{\rm e}$ [10^{-10} cm^{-3}]	86	161	0.016	1.7
s_1	2.1		1.1	1.6
s_2	3.0		3.4	3.7
$\gamma_{\rm min}$	1		1	
$\gamma_{\rm br}$	3.6×10^4		3.6×10^4	
$\gamma_{\rm max}$	3.3×10^5		3.3×10^5	
B [μG]	0.89		0.85	
$U_{\rm e}/U_{\rm B}$	4.3		1.8	
p [10^{-14} erg cm^{-3}]	5.6		2.7	

Table S1. Measured & model parameters for the Cen A giant lobes. The quoted distances are from the core to the centroid of the different regions. Errors in the flux and photon indices are statistical only – see Table S3 for a summary of the systematic errors.

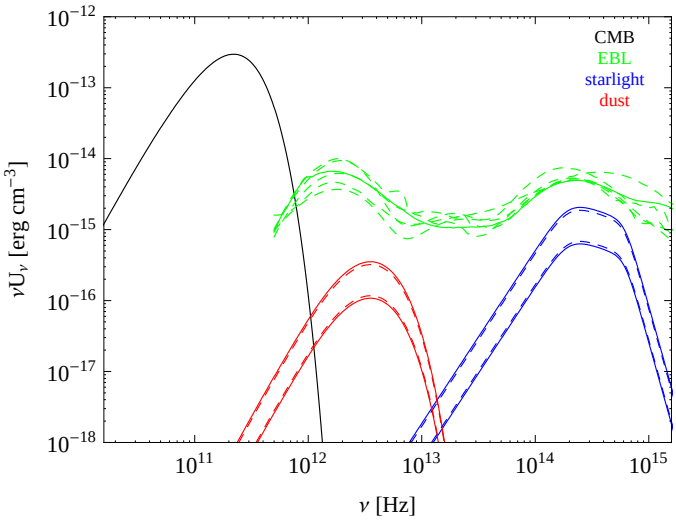

Fig. S2. Energy densities of different photon fields at the locations of the northern and southern giant lobes. For the EBL, the solid line indicates the compilation of (*S13*) utilized for the IC spectra in Fig. 3 of the main paper while the dashed lines are other EBL models considered (see Fig. S3). For the dust and starlight components, the solid lines are indicative of the northern regions (1 = lower, 2 = upper) and the dashed lines represent the southern regions (4 = upper, 5 = lower).

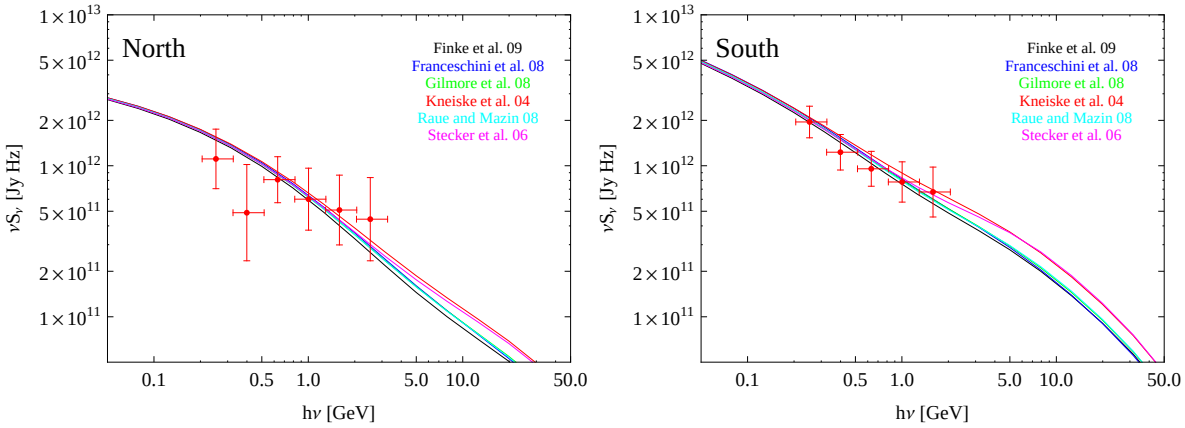

Fig. S3. Total IC fluxes of the northern [left] and southern [right] giant lobes computed for different EBL levels/spectral shapes, from (*S15*) (black lines), (*S16*) (blue), (*S17*) (green), (*S18*) (red), (*S13*) (cyan), and (*S19*) (magenta).

Name	$\alpha_{\rm J2000}$	$\delta_{\rm J2000}$
1FGL J1300.9−3745	$13^{\rm h}00^{\rm m}54^{\rm s}$	$-37°45'36"$
1FGL J1304.0−4622	$13^{\rm h}04^{\rm m}05^{\rm s}$	$-46°22'06"$
1FGL J1304.3−4352	$13^{\rm h}04^{\rm m}21^{\rm s}$	$-43°52'07"$
1FGL J1305.4−4928	$13^{\rm h}05^{\rm m}28^{\rm s}$	$-49°28'15"$
1FGL J1307.0−4030	$13^{\rm h}07^{\rm m}06^{\rm s}$	$-40°30'37"$
1FGL J1307.6−4259	$13^{\rm h}07^{\rm m}38^{\rm s}$	$-42°59'58"$
1FGL J1320.1−4007	$13^{\rm h}20^{\rm m}10^{\rm s}$	$-40°07'36"$
1FGL J1328.2−4729	$13^{\rm h}28^{\rm m}12^{\rm s}$	$-47°29'56"$
1FGL J1334.2−4448	$13^{\rm h}34^{\rm m}15^{\rm s}$	$-44°48'48"$
1FGL J1347.8−3751	$13^{\rm h}47^{\rm m}52^{\rm s}$	$-37°51'18"$
1FGL J1400.1−3743	$14^{\rm h}00^{\rm m}08^{\rm s}$	$-37°43'04"$

Table S2. Positions of point sources detected by the $Fermi$-LAT within the ROI that have been included in the background model.

Parameter	Value	Stat.	Sys. ($A_{\rm eff}$)	Sys. (diff.)	Sys. (radius)	Sys. (total)
Core flux	1.50	+0.25/–0.22	+0.12/–0.11	+0.02/–0.03	+0.35/–0.00	$\pm$0.37
Core index	2.67	+0.10/–0.10	+0.06/–0.06	+0.02/–0.00	+0.00/–0.05	$\pm$0.08
North lobe flux	0.77	+0.23/–0.19	+0.23/–0.16	+0.30/–0.14	+0.00/–0.09	$\pm$0.39
North lobe index	2.52	+0.16/–0.19	+0.18/–0.20	+0.11/–0.14	+0.06/–0.00	$\pm$0.25
South lobe flux	1.09	+0.24/–0.21	+0.25/–0.21	+0.14/–0.16	+0.00/–0.11	$\pm$0.32
South lobe index	2.60	+0.14/–0.15	+0.17/–0.15	+0.10/–0.05	+0.00/–0.01	$\pm$0.20

Table S3. Summary of statistical and systematic errors. The fluxes [10^{-7} ph cm^{-2} s^{-1}] quoted are in the > 100 MeV band. In addition to the statistical (Stat.) errors, the sources of systematic (Sys.) uncertainties are due to limited knowledge about the LAT effective area ($A_{\rm eff}$), variations of the diffuse model components (diff.), and core cut-out radius. Quoted are the minimum/maximum parameter differences from the values derived. The maximum values of each source of systematic error are added in quadrature to give the total systematic error.